Modeling of the free-electron recombination band in emission spectra of highly conducting *n*-GaN

B. Arnaudov,[1] T. Paskova,[2] E. M. Goldys,[3] S. Evtimova,[1] and B. Monemar[2]
[1]*Faculty of Physics, Sofia University, 5, J. Bourchier Boulevard, 1164 Sofia, Bulgaria*
[2]*Department of Physics and Measurement Technology, Linköping University, S-581 83 Linköping, Sweden*
[3]*Semiconductor Science and Technology Laboratories, Macquarie University, Sydney NSW 2109, Australia*
(Received 24 January 2001; published 9 July 2001)

We simulate the spectral distribution of the free-electron recombination band in optical emission spectra of GaN with a free-carrier concentration in the range of $5\times10^{17}-1\times10^{20}\,\mathrm{cm}^{-3}$. The influence of several factors, such as nonparabolicity, electron-electron interaction, and electron-impurity interaction on both the spectral shape and energy position and the effective gap narrowing are taken into account. The calculated properties of the free-electron-related emission bands are used to interpret the experimental photoluminescence and cathodoluminescence spectra of GaN epitaxial layers.

DOI: 10.1103/PhysRevB.64.045213 PACS number(s): 78.20.Bh, 78.60.Hk, 78.55.−m, 81.05.Ea

I. INTRODUCTION

Free-electron recombination across the band gap is typically observed in photoluminescence (PL) emission spectra in degenerate GaAs,[1–4] InP,[5,6] and InSb.[7] The spectral shape of the PL emission in these materials corresponds closely to the energy distribution of electrons in the conduction band, and its energy position can be explained by the interplay between the equilibrium Burstein-Moss shift[8] and the effective band-gap narrowing.

In ideal crystals the nonequilibrium electrons located in the vicinity of the quasi-Fermi level take part in radiative transitions, and these processes are described by the van Roosbroeck–Shockley relation.[9] However, in heavily doped and degenerate semiconductors,[10–12] due to the absence of long-range order, all electrons above the percolation level of the conduction band can participate in the radiative transitions, in apparent contradiction with simple rules for optical transitions. In this case the **k**-conservation principle is relaxed due to electron-electron and electron-impurity scattering processes, and thus all states occupied by electrons can take part in radiative transitions.[13] The most appropriate model describing this situation[1,2] assumes a free-to-bound recombination process, where the nonequilibrium holes due to their smaller Bohr radius are classically localized in a relatively narrow energy interval in the local potential minima of the valence-band edge.[10–12] In such free-to-bound recombination processes, a contribution from the light holes could, in general, be expected in the highest-energy part of the spectra. However, radiative transitions of the nonequilibrium light holes which are not localized in the potential relief were not observed, and usually were not discussed separately in the emission bands.[1–7] In some works[2] band-to-band and band-to-acceptor radiative recombination processes are included as well.

The contribution of the free-electron recombination band (FERB) in low-temperature near-band-edge (NBE) photoluminescence and spatially resolved cathodoluminescence (CL) spectra of hydride vapor phase epitaxial (HVPE) GaN was conclusively identified, and related to local unintentional doping nonuniformities and interface sublayers.[14–16] The FERB is usually superimposed over the strong excitonic peak characteristic of the higher quality parts of the film.

In our previous work[16] we have shown that by assuming the free-to-bound recombination mechanism a broad asymmetric NBE emission band observed in HVPE GaN can be modeled with good accuracy using sample parameters obtained in independent experiments. In this work, we theoretically simulate the spectral shape and energy of the FERB in highly conducting *n*-GaN, taking into account the influence of the conduction-band nonparabolicity, electron-electron interactions, electron-impurity interactions, and band-gap narrowing. The paper is organized in the following way: In Sec. II the theoretical model of the free-electron recombination is described in detail. Each subsection is devoted to separate terms of the general expression describing the FERB emission. In Sec. III the shape and energy position of the FERB are discussed, and the results in different approximations are analyzed in comparative way. In Sec. IV we compare our model predictions with the experimental spectra.

II. THEORETICAL MODEL OF THE FERB IN NEAR-BAND-EDGE EMISSION SPECTRA OF *n*-GaN

In this section, a model of free-electron radiative transitions in highly conducting *n*-GaN is presented in order to calculate the spectral distribution of luminescence at varying temperatures, electron concentrations, and compensation ratios. In the absence of wave-vector conservation, a general expression is used to describe the FERB intensity $I(h\nu)$ in degenerate *n*-GaN,[16]

$$I(h\nu)=\int_0^\infty\int_0^\infty W(E_n,E_p)n(E_n)p(E_p)\times\delta(E_n-E_p-E_g-h\nu)dE_n dE_p, \tag{1}$$

where

$$n(E_n)=g_n(E_n)f_n(E_n),\qquad p(E_p)=g_p(E_p)f_p(E_p). \tag{2}$$

Here $W(E_n,E_p)$ is the probability for radiative transitions; $n(E_n)$ and $p(E_p)$ are the energy distributions of electrons and holes, respectively; $g_n(E_n)$ and $g_p(E_p)$ are the semiclassical densities of states; f_n and f_p are the quasiequilibrium Fermi-Dirac functions; and $E_g=E_g(T)$ is the band-gap energy at a temperature T. The probability $W(E_n,E_p)$ is taken as a constant in a commonly used approximation.[1,2,5,10] All simulations are performed assuming the zero energy set at the bottom of the conduction band, $E_{co}=0$.

Various approximations of Eq. (1) were used previously for different III-V compounds[1–7] where either a δ-like, parabolic, or Gaussian energy distribution, or a nonquasiequilibrium behavior of the excited holes, were assumed. Conduction-band nonparabolicity and band tailing effects were included as well. In the following sections we will develop the model of the FERB for highly conducting GaN material, discussing and justifying all elements in Eq. (1).

A. Conduction-band density of states $g_n(E_n)$

Being a wide-band-gap material, GaN has a nearly parabolic density of states in the conduction band ($g_n \sim E_n^{1/2}$). In a strongly degenerate semiconductor, however, the Fermi energy is located high in the conduction band, and the density of states may, in principle, deviate from the simple parabolic dispersion law. The Mott transition in GaN takes place at an electron concentration of $(1.2–3.8)\times10^{18}\,\mathrm{cm}^{-3}$.[17,18] The three-band Kane model[19] is frequently used to describe the electron concentration dependence of the effective mass, density of states, and Fermi-level position, as well as their influence on the luminescence spectra.[2,5]

The energy dependence of the density of states effective mass m_n is described by the expression:[3,19]

$$\frac{1}{m_n}=\frac{1}{m_{n0}}\left(1-\alpha\frac{E_n}{E_g}\right). \tag{3}$$

Here m_{n0} is the electron effective mass at the bottom of the conduction band. The value of $m_{n0}=0.22m_0$ (Ref. 18) (m_0 is the free-electron mass) was used in our numerical calculations. The nonparabolicity parameter α can be described in the simplest, quasicubic approximation by the expression[19]

$$\alpha=\left(1-\frac{m_{n0}}{m_0}\right)^2\left[\frac{1+(\Delta/E_g)+(1/4)(\Delta/E_g)^2}{1+(4/3)(\Delta/E_g)+(4/9)(\Delta/E_g)^2}\right], \tag{4}$$

where Δ is the spin-orbit split-off band. Using the numerical values of $\Delta_{so}=18\,\mathrm{meV}$ obtained in a quasicubic approximation,[20] and $E_g=3503\,\mathrm{meV}$,[21] we obtained $\alpha=0.76$. The corresponding nonparabolic semiclassical density of states, g_n^{non}, is[19]

$$g_n^{\mathrm{non}}(E_n)=g_n(E_n)\left(1-\alpha\frac{E_n}{E_g}\right)^{-3/2}, \tag{5a}$$

where

$$g_n(E_n)=\frac{2\pi}{h^3}(2m_{n0})^{3/2}E_n^{1/2} \tag{5b}$$

and h is the Planck constant.

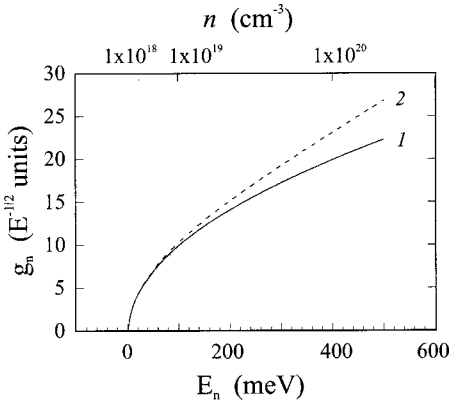

FIG. 1. Conduction-band electron density of states in GaN calculated in parabolic (curve *1*) and nonparabolic (curve *2*) approximations.

Figure 1 compares the parabolic (curve 1) and nonparabolic (curve *2*) density of states (in units of $E^{1/2}$) of the conduction band calculated using Eqs. (3)–(5). The electron densities corresponding to the Fermi energy E_{f0} at zero temperature are also shown in Fig. 1 (top scale). The effect of nonparabolicity on the density of states appears at the electron concentration of $\sim1\times10^{19}\,\mathrm{cm}^{-3}$, but the effect is smaller than 10% up to the concentration of $5\times10^{19}\,\mathrm{cm}^{-3}$, and becomes significant only at the highest limit of doping.

In highly doped semiconductors, the density of states in the band tails are characterized by the rms impurity potential G which, in the screened Coulomb potential approximation, is given by[10,11]

$$G=2\pi^{1/2}\frac{4\pi e^2}{\varepsilon R_s}(N_iR_s^3)^{1/2}. \tag{6}$$

where e is the electron charge, ε is the electric permittivity, and the total ionized impurity concentration N_i is related to the compensation ratio K through $N_i=(1+K)n$. The Thomas-Fermi screening length R_s in a degenerate electron gas in Eq. (6) is estimated using the following expressions:[11,12]

$$R_s=\left(\frac{\pi}{3}\right)^{1/6}\frac{a_B(e)}{2}[na_B(e)^3]^{-1/6}, \tag{7a}$$

$$a_B(e)=\frac{\varepsilon}{4\pi e^2}\frac{h^2}{4\pi^2m_n}. \tag{7b}$$

Here $a_B(e)$ is the effective Bohr radius of electrons. For electron concentrations above the Mott transition, the calculated values of R_s are smaller than $a_B(e)=2.5\times10^{-7}\,\mathrm{cm}$, which follows from the condition that Eq. (7) is valid when $[na_B(e)^3]^{-1/6}<1$. This condition is fulfilled when the mean distance between the majority carriers (and impurity atoms) becomes smaller than their Bohr radius. Usually the latter is expressed by the relation $na_B^3(e)>1$.[17]

Generally, the nonparabolicity may influence the screening length. For example in Ref. 5, a concentration-dependent screening length R_s^{non} was used in the calculation of the band shift due to the Coulomb interaction in heavily doped InP.

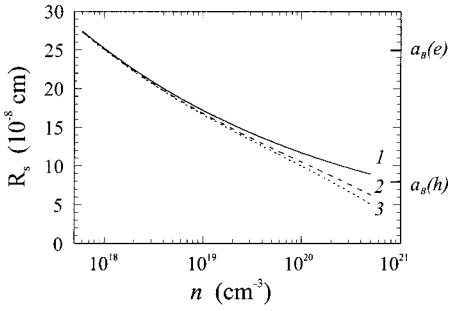

FIG. 2. The calculated dependence of the screening length on the electron concentration in parabolic (curve *1*) nonparabolic approximations according to Eq. (8) (curve *2*), and following Ref. 8 (curve *3*).

The concentration dependence appeared in the expression for the effective mass, and it was assumed that only the electrons near the Fermi level, E_f, take part in screening. In our work we calculate the concentration-averaged screening length, R_s^{mean}, using the expression

$$R_s^{\mathrm{mean}}=\frac{1}{E_f}\int_0^{E_f} R_s(E_n)dE_n, \tag{8}$$

where $R_s(E_n)$ is expressed by Eqs. (3) and (7).

Figure 2 shows the dependence of the screening length R_s on the electron concentration calculated in both parabolic and nonparabolic approximations. The parabolic curve *1* is calculated according to Eq. (7). The values of the screening length, R_s^{mean}, calculated according to Eq. (8) (curve *2*, Fig. 2) are compared with the values of R_s^{non} obtained using the method described in Ref. 5 (curve *3*, Fig. 2). The results show that the nonparabolicity leads to an effective decrease of the screening length, and that the effect is larger at higher free-carrier concentrations following the decrease of the effective Bohr radius according to Eqs. (3) and (7).

Figure 3 shows the relationship between the rms impurity potential G and the total ionized impurity concentration N_i at zero compensation ratio ($K=0$), also in both parabolic and nonparabolic approaches. The parabolic curve *1* (Fig. 3) was obtained using Eq. (6). Curves *2* and *3* (Fig. 3) present the

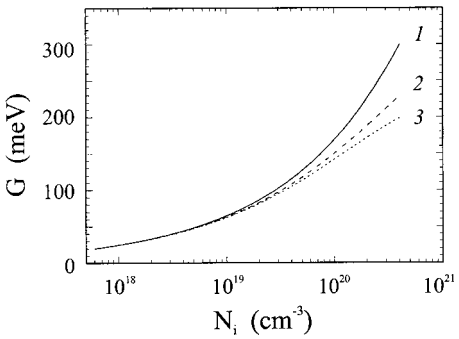

FIG. 3. The measure of the potential fluctuations G (rms) as a function of the total ionized impurity concentration calculated in the same three approaches as in Fig. 2.

calculated values of G in the nonparabolic approach according to Eq. (7), $G^{\mathrm{mean}}(R_s^{\mathrm{mean}})$, and in the approach of Ref. 5, $G^{\mathrm{non}}(R_s^{\mathrm{non}})$, respectively.

It can be seen from Figs. 1–3 that, up to concentrations $N_i=5\times10^{18}\,\mathrm{cm}^{-3}$ the three approximations are almost identical, and thus the nonparabolicity effect only slightly reduces the depth of the rms potential fluctuations. It is also important to point out that above $n=5\times10^{17}\,\mathrm{cm}^{-3}$ in all these cases, the obtained values of the rms impurity potential G are higher than kT even at 300 K ($\approx$26 meV). Therefore, the potential wells should localize the carriers. However, the majority carriers cannot occupy the potential wells near the conduction-band bottom due to the fact that the Bohr radius $a_B(e)$ is larger than the screening length, R_s. At the same time the heavy holes in GaN have a much smaller Bohr radius, which allows them to become localized and occupy the local potential extrema near the valence band top (see Sec. II D). Thus the optical transitions in the FERB take place between free electrons and localized holes.

The value of the rms impurity potential G is related to statistical fluctuations of the impurity and all charged point defect concentrations. These fluctuations lead to spatial variations of the band edges, and create tails in both conduction and valence-band densities of states. Assuming Gaussian fluctuations of the random impurity potential, a spatially averaged density of states g_s is given as[10–12]

$$g_s(E_n)=g_{n0}(E_n)\left(\frac{G}{E_n}\right)^{1/2}G_0\left(\frac{E_n}{G}\right), \tag{9}$$

where

$$G_0(x)=\pi^{-1/2}\int_{-\infty}^{x}[e^{-y^2}(x-y)^{1/2}]dy, \tag{10}$$

and the quantity x is the dimensionless energy $x=E_n/G$. The asymptotic properties of this density of states $g_s(x)$ are

$$g_s(x)\sim x^{1/2} \quad \text{at } x>2, \tag{11}$$

$$g_s(x)\sim e^{-x^2} \quad \text{at } x<0. \tag{12}$$

Thus the tailing effect on the density of states is negligible for energies higher than $2G$ in the conduction band, within the range of interest in the case of degenerate doping.

We calculate the energy dependencies of the average density of states $g_s(E_n)$ in GaN for two impurity concentrations of 2.5×10^{19} and $5\times10^{19}\,\mathrm{cm}^{-3}$ at zero compensation ($K=0$) in both the parabolic (g_s) and nonparabolic (g_s^{non}) approximations. The effect of nonparabolicity on the conduction-band tailing is taken into account in Eqs. (9) and (10), where $g_n(E_n)$ is replaced by $g_n^{\mathrm{non}}(E_n)$ according to Eq. (5).

In Fig. 4(a) we show the calculated parabolic (curve *1*, solid line) and nonparabolic (curve *2*, dashed line) average densities of states for $N_i=2.5\times10^{19}\,\mathrm{cm}^{-3}$. For comparison, the unperturbed parabolic (curve *3*, dotted line) and nonparabolic (curve *4*, dash-dotted line) density of states are shown in the same figure. The close coincidence of the perturbed and unperturbed curves *1* and *3* as well as curves *2* and *4*, for

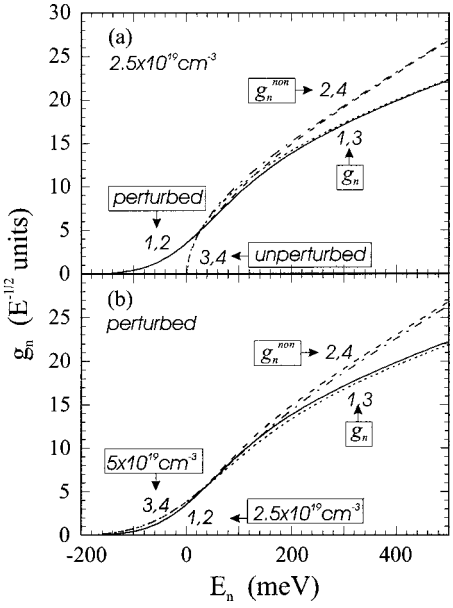

FIG. 4. (a) Comparison between the spatially averaged conduction-band density of states including tails in GaN for an impurity concentration of $N_i=2.5\times10^{19}\,\mathrm{cm}^{-3}$ calculated in the parabolic (curve *1*, solid line) and nonparabolic (curve *2*, dashed line) cases, and the corresponding unperturbed parabolic (curve *3*, dotted line) and nonparabolic (curve *4*, dash-dotted line) DOS's. (b) The conduction-band DOS including tails calculated for an impurity concentration of $N_i=2.5\times10^{19}\,\mathrm{cm}^{-3}$ in the parabolic (curve *1*, solid line) and nonparabolic (curve *2*, dashed line) approximations compared with the corresponding conduction-band DOS including tails calculated for the impurity concentration of $5\times10^{19}\,\mathrm{cm}^{-3}$ in the same approximations (curve *3*, dotted line, and curve *4*, dash- dotted line, respectively).

energies higher than 40 meV, means that for degenerate electron concentrations ($>5\times10^{18}\,\mathrm{cm}^{-3}$) in GaN the tailing does not affect the density of states (DOS). The tailing strongly influences the DOS in the range of negative energies, as observed in Fig. 4(a). These tail states are statistically distributed in energy according to the Gaussian law due to conduction-band-edge fluctuations, and curves *1* and *2* [Fig. 4(a)] show their Gaussian envelope.

Further, in order to reveal the effect of variation of impurity concentration on the tailing, in Fig. 4(b) we plot the calculated curves that describe the tailing for two ionized impurity concentrations of 2.5×10^{19} and $5\times10^{19}\,\mathrm{cm}^{-3}$. The parabolic curve *1* (solid line) and nonparabolic curve *2* (dashed line) DOS's correspond to an impurity concentration of $2.5\times10^{19}\,\mathrm{cm}^{-3}$. Curves *3* (dotted line) and *4* (dash-dotted line) are calculated for an impurity concentration of $5\times10^{19}\,\mathrm{cm}^{-3}$ in the parabolic and nonparabolic cases, respectively. There is a similar shift between the curves *1* and *3* and curves *2* and *4*, respectively, for energies higher than 100 meV, indicating the similarity of the impurity concentration effect in the parabolic and nonparabolic cases. It is also seen in the Fig. 4(b) that the DOS increases with increasing impurity concentration for $E_n\leqslant50$ meV (curves *3* and *4* are higher than curves *1* and *2*), indicative of an enhancement of the tailing effect in this energy region.

Inspection of Figs. 4(a) and 4(b) shows that the effects of the nonparabolicity and impurity concentration increase are both of importance for band tailing below the unperturbed conduction-band edge E_{c0}. However, as mentioned earlier, the tail states can not be occupied by electrons due to the disparity between the electron Bohr radius and the screening length. Therefore, we conclude that electrons participating in the radiative recombination are free above the percolation level in the conduction band. This fact allows us to neglect the band-tailing effects in the conduction-band density of states in Eq. (1). In our further considerations we will use the density of states g_n and g_n^{non}, as shown in Fig. 1.[22]

B. Fermi-Dirac distribution for electrons $f_n(E_n)$

The Fermi-Dirac distribution for electrons depends on the quasi-Fermi level and on the effective carrier temperature. The location of the quasi-Fermi level depends on excitation conditions, namely, the generation rate and the minority-carrier lifetime. Typically in our experiment we used the PL excitation power density $P_s\approx100\,\mathrm{W/cm}^2$. Assuming an effective absorption length of 0.1 μm and a low-temperature carrier diffusion length in the order of 0.1 μm, and using the lifetime value of 0.5 ns, we obtain the non-equilibrium carrier concentration of less than $5\times10^{15}\,\mathrm{cm}^{-3}$. In the CL experiments an electron-beam energy of 15 keV was typically used, electron-beam currents were in a range between 1 and 5 nA, and the excitation spot of the order $1\times1-2\times2\,\mu\mathrm{m}^2$, giving $P_s\approx3\times10^3\,\mathrm{W/cm}^2$. These excitation power values may lead to a nonequilibrium carrier concentration of about $10^{16}\,\mathrm{cm}^{-3}$.

At these low nonequilibrium carrier densities related to low-excitation conditions, the electron quasi-Fermi level in Eqs. (1) and (2) coincides with the Fermi energy E_f, and is nearly equal to the zero temperature value E_{f0} corrected by the first-order temperature term $\Delta_{f\text{-}t}(kT\ll E_{f0})$:

$$\Delta_{f\text{-}t}=\frac{1}{2}\,\pi^2\left(\frac{kT}{E_{f0}}\right)^2. \tag{13}$$

The precise behavior of the Fermi-Dirac function may also be affected by lifetime variations of the nonequilibrium carriers or by the elevated electron temperatures of the majority carriers, as recently reported by Binet and Duboz.[18] In the case of such high quasiequilibrium carrier concentration, the equilibrium functions f_n and f_p, described by the quasi-Fermi levels E_{fn} and E_{fp}, will correspond to an effective temperature Θ of the carriers, which can be significantly higher than the lattice temperature, *T*. This phenomenon was observed in the CL FERB spectra of GaAs reported in our previous work.[1] Based on a similar experimental model for GaN, we can expect values of the electron temperature Θ even in the range of 50–80 K at the experimental conditions of our PL and CL experiments. The effect of the electron temperature increase is more pronounced in low-temperature experiments, and becomes negligible at room temperature.

According to Eqs. (1) and (2), the electron temperature Θ is reflected in the high-energy slope of the spectra via f_n, and the hole temperature is reflected in the low-energy slope

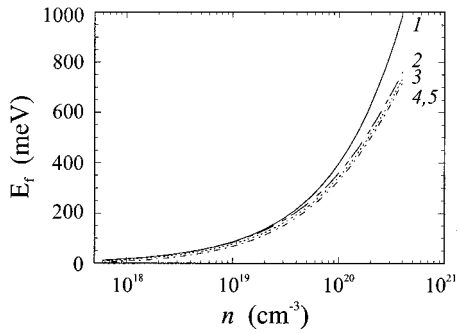

FIG. 5. The Fermi energy as a function of the electron concentration calculated in the following approximations: parabolic (curve *1*, solid line); nonparabolic (curve *2*, dash-dotted line); nonparabolic, including electron-electron interactions (curve *3*, dotted line); nonparabolic, including electron-electron and electron-impurity interactions (curve *4*, dashed line); and nonparabolic, with electron-electron, electron-impurity, and temperature corrections (curve *5*). Curve *5* coincides with the curve *4*.

via f_p, respectively. Thus the electron and/or hole temperature can be independently estimated from the experimental results.

Now we consider the effect of nonparabolicity on the Fermi-Dirac distribution. According to Eq. (3) we calculate the Fermi energy $E_f^{\rm non}$ in the nonparabolic conduction band using the following expression:[19]

$$E_{f0}^{\rm non}=E_{f0}\left(1-\alpha\frac{E_{f0}}{E_g}\right). \tag{14}$$

Figure 5 shows the evolution of the Fermi energy E_{f0} with increasing electron concentration in the parabolic (curve *1*) and nonparabolic (curve *2*) approximations in the concentration range of $5\times10^{17}-5\times10^{20}\,{\rm cm}^{-3}$. The nonparabolicity effect starts to be noticeable for concentrations higher than $n=10^{19}\,{\rm cm}^{-3}$. It is interesting that this effect in GaN is rather small compared to other III-V compounds investigated previously.[2,5]

We further consider the electron-electron interactions which lead to lowering of the Fermi energy by the value of $\Delta_{e\text{-}e}$, according to the expressions[12]

$$E_{f0e}^{\rm non}=E_{f0}^{\rm non}-\Delta_{e\text{-}e},$$

$$\Delta_{e\text{-}e}=3^{-1/3}\pi^{-5/3}a_B^{-1}n^{-1/3}E_{f0}. \tag{15}$$

These relationships are applicable when the mean distance between the majority carriers becomes smaller than their Bohr radius. Curve *3* in Fig. 5 shows the calculated values of the Fermi energy for highly conducting *n*-GaN. The correction of the Fermi-level position due to electron-electron interaction is very small for all carrier concentrations of interest.

Interactions of electrons with impurities affect the Fermi energy as well. Lowering of the Fermi energy $\Delta_{e\text{-}i}$ due to the conduction band tailing takes place, together with changes of the density of states [Eq. (8)], as described by the following expressions:[11,12]

$$E_{f0e\text{-}i}^{\rm non}=E_{f0}^{\rm non}-\Delta_{e\text{-}i}, \tag{16a}$$

$$\Delta_{e\text{-}i}=\frac{1}{8}\frac{G^2}{E_{f0}}. \tag{16b}$$

Since in degenerate semiconductors the rms potential fluctuation G is always smaller than the Fermi energy ($G<E_{f0}$),[11] the Fermi-level lowering is also small. Curve *4* in Fig. 5 shows the calculated values of the Fermi energy in *n*-GaN using this correction as well.

We also considered the lattice temperature correction [Eq. (13)] plotted in Fig. 5, curve *5*. Curve *5* coincides with the curve *4*, which indicates that the temperature correction is negligible.

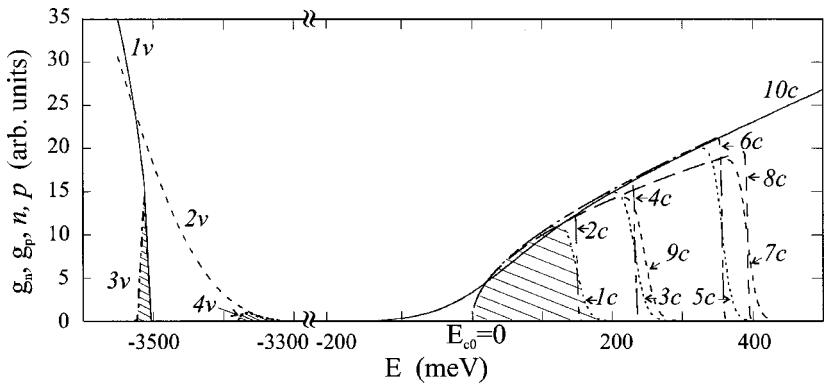

FIG. 6. Right: Electron distributions $n(E_n)$ in the conduction band for three electron densities—$2.5\times10^{10}\,{\rm cm}^{-3}$ (curves $1c$ and $2c$), $5\times10^{19}\,{\rm cm}^{-3}$ (curves $3c$ and $4c$), $1\times10^{20}\,{\rm cm}^{-3}$ (curves $5c$ and $6c$)—calculated in nonparabolic approximation at two electron temperatures $\theta=80$ K (dotted lines) and $\theta=2$ K (broken-dotted lines). Parabolic electron distributions for $n=1\times10^{20}\,{\rm cm}^{-3}$ and $\theta=80$ K (curve $7c$); for $n=1\times10^{20}\,{\rm cm}^{-3}$ and $\theta=2$ K (curve $8c$), and for $n=5\times10^{19}\,{\rm cm}^{-3}$ and $\theta=80$ K (curve $9c$), are plotted with dashed lines. The nonparabolic density of states $g_n^{\rm non}(E_n)$, including tails calculated for $n=2.5\times10^{19}\,{\rm cm}^{-3}$ (curve $10c$, solid line) is also shown for comparison Left: Parabolic density of states $g_p(E_p)$ (curve $1v$) and parabolic density of states including tails $g_{ps}(E_p)$ (curve $2v$) in the valence band. The quasiequilibrium hole distribution $p(E_p)$ at $\theta=2$ K (curve $3v$) and the nonquasiequilibrium hole distribution $p_s(E_p-E_a)$ for $N_i=2.5\times10^{19}\,{\rm cm}^{-3}$ (curve $4v$) are also shown.

C. Electron energy distribution

The electron distribution $n(E_n)$ is calculated according to Eqs. (1) and (2). $n(E_n)$ is obtained using the Fermi energy value E_{fn}, taking into account the corrections (13)–(16) for the electron temperature Θ.

Figure 6 (right panel) shows the calculated energy distributions of electrons at three electrons densities of 2.5×10^{19}, 5×10^{19}, and $1\times10^{20}\,\mathrm{cm}^{-3}$ in the nonparabolic approximation for two electron temperatures $\Theta_1=2$ K and $\Theta_2=80$ K. Curves *1c* and *2c* present the electron distributions in the conduction band for $n=2.5\times10^{19}\,\mathrm{cm}^{-3}$ at $\Theta_1=80$ K and $\Theta_2=2$ K respectively; curves *3c* and *4c* are obtained for $n=5\times10^{19}\,\mathrm{cm}^{-3}$ at the same two electron temperatures; and curves *5c* and *6c* are the corresponding electron distributions for $n=1\times10^{20}\,\mathrm{cm}^{-3}$ and also for two electron temperatures Θ_1 and Θ_2. For comparison, the calculated parabolic energy distributions of electrons for $n=1\times10^{20}\,\mathrm{cm}^{-3}$ at $\Theta_1=80$ K (curve 7*c*) and $\Theta_2=2$ K (curve 8*c*), as well as for $n=5\times10^{19}\,\mathrm{cm}^{-3}$ at $\Theta_1=80$ K (curve 9*c*), are plotted in Fig. 6. The nonparabolic density of states including tails g_s^{non} calculated for $N_i=2.5\times10^{19}\,\mathrm{cm}^{-3}$ (curve 10*c*) is presented in the figure as well.

As shown in Fig. 6, the difference between the nonparabolic and parabolic electron energy distributions becomes more pronounced at $n>5\times10^{19}\,\mathrm{cm}^{-3}$ (see, for example, curves *3c* and *9c*), but it is noticeable even at lower concentrations. The Fermi-level position is more strongly affected by nonparabolicity, because its lowering can be observed even at $n=5\times10^{19}\,\mathrm{cm}^{-3}$ (see, for example, curves *3c* and *9c*). The shape of the conduction-band DOS occupied by electrons does not differ much between the parabolic and nonparabolic cases. Moreover, the filling of the conduction band with electrons is not influenced by the density of states tailing. This fact is illustrated in Fig. 6, where the low-energy sides of curves *10c* and $3c-6c$, calculated for electron concentrations higher than $5\times10^{19}\,\mathrm{cm}^{-3}$, nearly coinside.

D. Valence-band density of states $g_p(E_p)$

We first discuss the influence of nonparabolicity on the valence-band density of states g_n. The concentration of minority carriers (holes) in *n*-GaN is low, and the effective mass of the heavy holes (averaged between the longitudinal and transverse effective mass values) $m_{p0}\approx0.8m_0$ (Ref. 18) is higher than the electron effective mass. Thus both equilibrium and nonequilibrium holes are localized in a very narrow energy interval near the valence-band edge. Consequently, we can neglect the nonparabolicity effects on the valence band density of states. The values of the nonparabolic valence band density of states $g_p^{\mathrm{non}}(E_p)$ calculated according to Eq. (4), where E_n is replaced by the energy of holes E_p (shifted by $-E_g$), and m_{n0} is replaced by the heavy-hole effective mass m_{p0}, coincide with the parabolic densities of states $g_p(E_p)$ in the entire energy region. We use the parameters of heavy holes only, and neglect the light holes, since the former are exclusively responsible for the position of the Fermi energy in the valence band. It is thus justified to calculate the parameters of the FERB using the valence-band density of states in the parabolic approximation.

The valence-band density of states in highly doped GaN is described by Eqs. (5) and (9), respectively, in a reversed energy scale, and with E_n replaced by E_p. The hole density of states in a parabolic valence band is shown by curve *1v* (solid line) in Fig. 6 (left panel). The calculated DOS in the parabolic approximation including band tails is also presented in Fig. 6 by curve *2v* (dashed line). It is seen that the density of states $g_{ps}(E_p)$ is well described by a Gaussian curve in the energy region lower than $E_v=-E_g=-3503$ meV ($T=2$ K).

The effective Bohr radius of heavy holes $a_B(h)=7\times10^{-8}$ cm is smaller than the screening length R_s, leading to a localization of holes in the valence-band potential fluctuations. At the same time, the potential relief depth *G* and screening length R_s (as well as the zero temperature Fermi level E_{f0}) are defined by the majority carrier parameters according to Eqs. (6) and (7). Thus the tailing effects near the valence-band edge are significant and need to be accounted for in the model.

E. Fermi-Dirac function $f_p(E_p)$ and the energy distribution $p(E_p)$ for holes

The estimated Mott transition hole density according to the value of m_{p0} is higher than $9\times10^{19}\,\mathrm{cm}^{-3}$, and the holes (both equilibrium and nonequilibrium) are not degenerate in the entire range of densities under investigation. Within the quasiequilibrium description of band-to-band radiative transitions[2,5] the quasi-Fermi level for holes, E_{fp}, in the parabolic valence band is located deep in the energy gap. The corresponding energy distribution of holes $p(E_p)$ at $\Theta=2$ K is shown in Fig. 6 (left panel) by curve *3v* (dash-dotted line). As it is well known, the curve *3v* presents a nondegenerate carrier distribution with a full width at half maximum of about $kT/2$ (Ref. 22) above the unperturbed valence band bottom.

Since the valence-band edge is perturbed by statistical potential fluctuations and the screening length is larger than the hole Bohr radius, $R_s>a_B(h)$, both equilibrium and nonequilibrium heavy holes are classically localized in the acceptorlike minima of the valence-band tails. Therefore the recombination processes are best modeled as free-to-bound carrier radiative transitions (FERBs).[1,11,16]

The band-tail states formed by the potential relief minima (or maxima in the case of the valence band edge) are spatially localized, and the distribution of nonequilibrium holes cannot be described using the concept of a quasi-Fermi level for the entire sample volume.[11] The participating nonequilibrium holes at low excitation conditions occupy the tail states below the energy level of thermal delocalization, E_a (Refs. 1 and 23):

$$E_a=-E_g+\sqrt{2}G. \tag{17}$$

It was previously shown[1,14,16,24] that the experimentally observed FERB's in GaAs, InP, and GaN can be well described by a similar theory when the nonequilibrium distribution function for holes was assumed to be of Fermi-Dirac type with the quasi-Fermi level f_p replaced by E_a. In a

similar way we apply this non-quasiequilibrium approach to GaN, and compare it with the quasiequilibrium approach.

The calculated nonquasiequilibrium distribution of holes $p_s(E_p-E_a)=g_{ps}f_p(E_a)$ for impurity densities of $N_i=2.5\times10^{19}\,\mathrm{cm}^{-3}$ is shown by curve *4v* (dotted line) in Fig. 6 (left panel). We can see that in the nonequilibrium approach the holes are distributed in a wider and deeper energy interval compared with the quasiequilibrium situation. Moreover, the low-energy shift of the occupied tail states is determined by the ionized impurity concentration in the sample.

III. DISCUSSION

A. FERB shape. Compensation and temperature effects

The analysis of the curves presented in Fig. 6 shows that the electrons taking part in radiative transitions occupy a wide range of energies, E_n, up to 250 meV above the conduction band edge for $n=5\times10^{19}\,\mathrm{cm}^{-3}$ while the nonequilibrium holes are distributed in a narrow energy interval (ΔEp), of the order of 10–50 meV [where the lower limit of ΔEp is determined by the quasiequilibrium function (curve *3v*)]. Therefore, the FERB intensity $I(h\nu)$, calculated according to Eq. (1), reflects essentially the energy distribution $n(E_n)$ as shown by curves *1c–9c*.

Further we calculate the FERB shape in GaN using Eq. (1) with an electron energy distribution $n(E_n)$ corresponding to curves *1c–6c* in Fig. 6 (right panel) for electron concentrations of 2.5×10^{19}, 5×10^{19}, and $1\times10^{20}\,\mathrm{cm}^{-3}$. The calculations are performed in a nonparabolic approximation, taking into account the effects of electron temperature ($\Theta=2$ and 80 K), quasiequilibrium and nonquasiequilibrium hole distribution, from here onward called quasiequilibrium and nonquasiequilibrium cases, and for the two values of impurity compensation *K*, namely, $K=0$ and 0.5.

Curves *1–3* (solid lines) in Fig. 7(a) show the calculated spectral shape in the quasiequilibrium case for the same three electron concentrations at $\Theta=2$ K. Curves *4–6* (dotted lines) in the same figure present the corresponding calculated spectral shapes for $\Theta=80$ K. Actually, this approach presents the spectral shape of indirect band-to-band radiative transitions[2] proposed to be a possible mechanism for electron-hole plasma recombination in GaN.[25,26] We note that the emission band shapes shown in Fig. 7(a) nearly reproduce the curves *1c–6c* from Fig. 6 (normalized to unity).

Figure 7(b) illustrates the effect of electron temperature on the spectral shape in the nonquasiequilibrium case for electron energy distribution at the same three electron concentrations. The curves are labeled in correspondence to those in Fig. 7(a), and they are plotted on the same scale. It can be seen that in the non-quasiequilibrium case the high-energy slope is not very sharp compared to that in the quasiequilibrium case [see Fig. 7(a)], even at a low electron temperature $\Theta=2$ K. The difference between the curves in Fig. 7(a) and 7(b) is more important at lower emission intensity, where a specific bump can be observed due to valence band tailing.

Figure 7(c) compares the results of the quasiequilibrium approach (curves *1–3*, solid lines), with the nonquasiequilibrium ones (curves *4–6*, dotted lines) at a certain electron temperature $\Theta=80$ K. It is seen that the valence-band tailing included in curves *4–6* makes both high and low-energy slopes more gentle. We point out that the curves *4–6* account for the radiative transitions participated in only by heavy

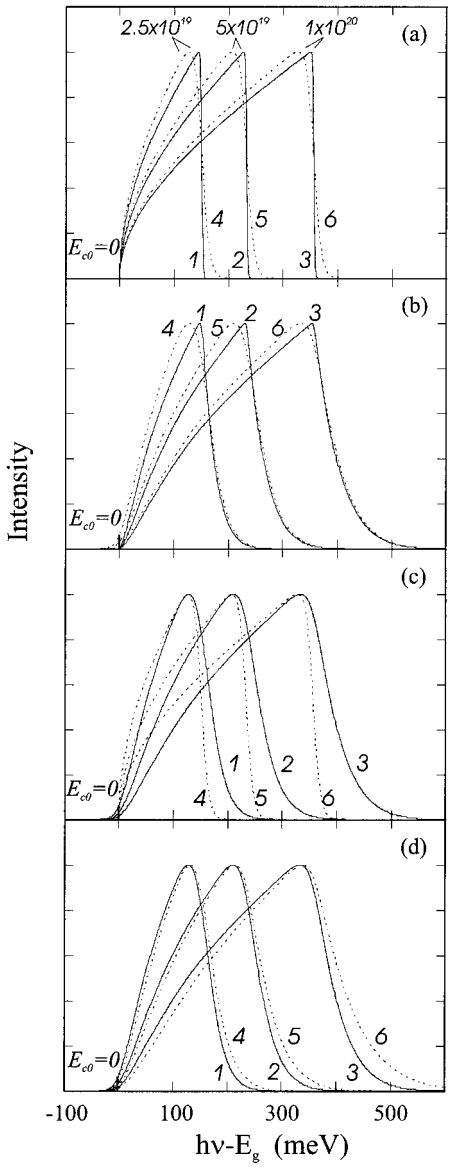

FIG. 7. (a) Calculated FERB spectral shape in the quasiequilibrium approach at $\theta=2$ K for three electron densities: $2.5\times10^{19}\,\mathrm{cm}^{-3}$ (curve *1*, solid line), $5\times10^{19}\,\mathrm{cm}^{-3}$ (curve *2*, solid line) and $1\times10^{20}\,\mathrm{cm}^{-3}$ (curve *3*, solid line) compared with the corresponding curves *4–6* (dotted lines) calculated at $\theta=80$ K and zero compensation ratio. (b) Calculated FERB spectral shape in the nonquasiequilibrium approach. Curves 1–6 correspond to the conditions in (a). (c) A comparison between the FERB spectral shape calculated in the quasiequilibrium approach (curves *1–3*, solid lines) with the nonquasiequilibrium ones (curves *4–6*, dotted lines) at a certain electron temperature $\theta=80$ K and zero compensation for the same three electron concentrations. (d) Compensation effect on the FERB spectral shape: curves *1–3* (solid lines), calculated at $\theta=80$ K and zero compensation, $K=0$; curves *4–6* (dotted lines), calculated at $\theta=80$ K and $K=0.5$ for the same three electron concentrations.

holes. The unlocalized light holes are located higher in the valence-band DOS (see Fig. 6, left panel, curve $3v$) and thus the radiative transitions should influence the highest-energy part of the spectra. In particular, they should appear at higher energies than the high-energy slope of curve $1c$ in Fig. 6, and subsequently in the high-energy side of the spectral shape of curve *4* in Fig. 7(c).

Finally, Fig. 7(d) reveals the effect of compensation on the spectral shape in the nonquasiequilibrium case, since generally the spectral shape in the quasiequilibrium case is not affected by the impurity concentration. Here curves *1–3* (solid lines) are calculated for the same three electron concentrations at $\Theta = 80$ K and zero compensation ($K = 0$), and compared with the corresponding curves *4–6* (dotted lines) calculated at a compensation ratio $K = 0.5$. One can see that the high-energy slope becomes additionally less inclined due to the increase of G with increasing compensation ratio K.

As shown in Figs. 7(a)–7(d) the nearly parabolic low-energy side of the emission band maintains its shape at the higher-intensity region in all approximations used. The nonparabolicity changes the local curvature only slightly. Thus we obtain that the unperturbed conduction-band edge E_{c0} can be set at a zero-energy position in all simulations by extrapolating the parabolic part of the low-energy spectral side to zero intensity.

The high-energy side of the FERB behaves similarly to the Fermi-Dirac-like function described by Eq. (1). The exponential parameter in this function comprises the kT (or $k\Theta$) parameter in f_n and $G(N_i)$ from the Gaussian part of g_{ps} in the nonquasiequilibrium case. Thus the high-energy slope of the emission band accounts for both the electron temperature and impurity concentration effects.

Comparing the calculated curves shown in Fig. 7, we conclude that the nonquasiequilibrium approach leads to a more realistic spectral shape of the high-energy side as well as the low-energy side at the lowest emission intensity. Moreover, the spectral shape calculated taking into account the valence-band tailing is sensitive to the impurity concentration, as demonstrated in Fig. 7(d). Thus, by numerical modeling of the spectral shape, and varying the values of E_f, Θ, G, and K to obtain the best fit to the experimental FERB shape, we can derive the Fermi energy and electron concentration values.[14,16] It should be emphasized that precise numerical simulation of the spectral shape including all corrections can yield the value of the electron concentration with a few percent accuracy.

As discussed above, the high-energy side of the emission band reproduces the Fermi-Dirac function for electrons. The energy position of the radiative transition from the Fermi level corresponds closely to the energy $E(I_{1/2})$ at 50% intensity at low temperatures.[1,27] At higher temperatures as well as at increased compensation, the Fermi-level transition position shifts slightly to higher intensity, although it is always lower than the energy at maximum PL intensity $E(I_{\max})$, and needs to be estimated numerically. We note that the comparison between the experimentally measured value $E(I_{1/2})$ (when the E_{c0} position is set at zero) and the calculated Fermi-energy position in the conduction band [Eq. (16)] can be used as a first approximation in the estimate of the electron density from the near-band-edge emission spectra. Moreover, in order to obtain the electron concentration (with about 10% accuracy), in this case we can use the simplest quasiequilibrium approach with a δ-like hole energy distribution. Further we can estimate the Fermi energy E_f and calculate the free-electron concentration n by extrapolating the nearly parabolic low energy side to zero-intensity energy $E_{c0} = 0$ and deriving the half-intensity energy $E(I_{1/2}) - E_{c0}$ from the high-energy side.

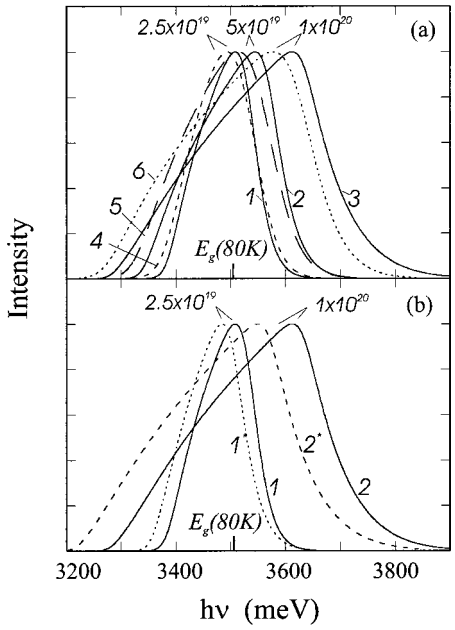

FIG. 8. (a) FERB spectral distributions in the nonquasiequilibrium approach at $T = \theta = 80$ K. Curves *1–3* (solid lines) are calculated at zero compensation, $K = 0$, for the three electron concentrations as given in Fig. 7. Curves *4–6* (dashed lines) are the respective ones calculated at $T = \theta = 150$ K. (b) Compensation effect on the FERB spectral distribution: curves *1* and *2* (solid lines) calculated at zero compensation ratio $K = 0$ for two electron densities 2.5×10^{19} and 1×10^{20} cm^{-3}: curves *1** and *2** (dashed lines) calculated for the same electron concentrations at compensation ratio $K = 0.5$ ($T = \theta = 80$ K).

B. FERB energy position

The calculation of the FERB energy position includes band-gap renormalization. We analytically calculate the effective band-gap value using Eq. (1), as in our previous work concerned with a FERB analysis in GaAs.[1,2] We point out that this procedure is applicable only to the nonquasiequilibrium case, although it was performed as a separate procedure in the quasiequilibrium approach.[5,28]

Following Eqs. (1) and (17), all radiative transitions responsible for the FERB are reduced in energy by the value of $E_a(N_i)$, with respect to the valence-band edge $E_v = -E_g(T)$. Equation (17) describes the actual temperature and impurity-related gap renormalization, and thus the energy position of the emission band. In the present simulation we use the band-gap energy renormalized after Eq. (17) in order to evaluate both impurity concentration and compensation ratio effects on the FERB spectral energy position.

We point out that Eq. (7) defines the spatially averaged optical gap shrinkage due to impurity potential fluctuations, and not fundamental gap energy reduction.[10,11] The latter is strongly affected by lattice temperature. Thus by fitting both parameters $G(N_i)$ and T in addition to the band-gap energy E_g in the nonquasiequilibrium case, we simultaneously obtain both the spectral shape and energy position of the FERB simply using Eqs. (1) and (17) without any additional operations.

Curves *1–3* in Fig. 8(a) show the energy position of FERB emission spectra calculated for three electron concentrations 2.5×10^{19}, 5×10^{19}, and $1\times10^{20}\,\mathrm{cm}^{-3}$, respectively, assuming zero compensation $K=0$ $(n=N_i)$ and equal lattice and electron temperatures $T=\Theta=80\,\mathrm{K}$. These three curves were shown in Fig. 7(d) when their low energy slope was centered at $E_{c0}=0$. In Fig. 8(a) we show that when the electron and/or impurity concentration increases the low energy side extrapolated to zero-intensity (E_{c0}) is shifted to lower energies with respect to the $E_g(80\,\mathrm{K})=3500\,\mathrm{meV}$.[29] The spectral energy position is a good indicator of the actual sample temperature, and can be used to determine the impurity concentration as well. Thus in the simulation procedure, it is possible to estimate the influence of both lattice temperature T and electron temperature Θ on the FERB spectral position either via the temperature gap shrinkage or via the high-energy spectral slope. If the temperature obtained from the band-gap shrinkage coincides with the temperature determined from the Fermi-Dirac-like high-energy slope, we can conclude that the lattice and electron temperatures are equal: $T=\Theta$.

Curves *4–6* in the same figure reveal the effect of higher lattice and electron temperature on the shape and energy position of the FERB emission. Curves *4–6* correspond to curves *1–3* calculated at $T=\Theta=150\,\mathrm{K}$. It can be seen that both temperatures independently affect the FERB emission. The lattice temperature T influences the energy position of the FERB following the band-gap reduction, while the electron temperature Θ mainly affects the shape of the FERB emission, as also observed in Fig. 7.

Figure 8(b) presents the effect of compensation on the FERB emission energy positions. Curves *1* and *2* are calculated at zero compensation ratio, $K=0$, and at $T=\Theta=80\,\mathrm{K}$ for two electron concentrations 2.5×10^{19} and $1\times10^{20}\,\mathrm{cm}^{-3}$, respectively. The corresponding curves *1** and *2**, calculated at $K=0.5$, are significantly shifted to lower energies. If the electron temperature coincides with the lattice temperature, we can attribute this additional gap shrinkage to the presence of an excess of impurity concentration, i.e., to higher compensation, $K>0$. In such a case, it is necessary to compare the value of G corresponding to the measured gap shrinkage with the exponential slope value of the high-energy spectral side. When they coincide, the compensation ratio K can be calculated from the experimentally derived values of $G(N_i)$ and $E_f(n)$.

In addition, a comparison between the curve shifts in Figs. 8(a) and 8(b) reveals that the shift due to compensation increase is very strong (26 meV for $n=2.5\times10^{19}\,\mathrm{cm}^{-3}$ and 50 meV for $n=1\times10^{20}\,\mathrm{cm}^{-3}$) while the temperature-related band-gap shrinkage is almost negligible (3 meV even at such a high temperature as $T=\Theta=150\,\mathrm{K}$). Thus the compensation effect seems to be dominant for the FERB energy position.

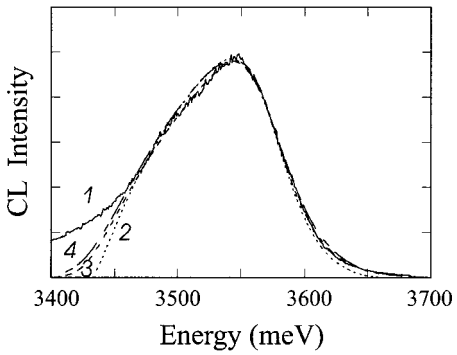

FIG. 9. Low-temperature (7 K) spatially resolved CL spectrum (curve *1*, solid line) taken in a defective region of thick GaN film (Ref. 16) compared with the calculated FERB emission spectra for highly conducting *n*-type GaN. Curve *2* (dotted line) is calculated in the parabolic approximation for $n=2.5\times10^{19}\,\mathrm{cm}^{-3}$. curve *3* (dashed line) is calculated in the nonparabolic approximation for $n=2.65\times10^{19}\,\mathrm{cm}^{-3}$ and $\theta_e=\theta_h=52\,\mathrm{K}$. Curve *4* (dash-dotted line) is calculated in the nonparabolic approximation for $n=2.65\times10^{19}\,\mathrm{cm}^{-3}$, $\theta_e=52\,\mathrm{K}$, and $\theta_h=100\,\mathrm{K}$.

We note that the simulations discussed in Secs. III A and III B and III D offer a contactless method to determine the electron concentration and compensation ratio in highly conducting GaN based on the FERB shape and energy position analysis. The method is an alternative to that based on Raman-scattering (RS) phonon-plasmon modes analysis or to routine resistivity and Hall mobility measurements. The accuracies of the both FERB analysis and Hall method are comparable. The Hall-scattering factor involves at least a 5% uncertainty in addition to the sample thickness measurement error. Both the shape and energy position of the FERB can be fitted pricisely which leads to a high accuracy in the range of applications.

IV. COMPARISON WITH EXPERIMENT

NBE luminescence spectra of unintentionally doped,[14–16,26,27] silicon doped,[28,30] and highly-excited[18] epitaxial GaN in the temperature range 2–300 K were investigated by many groups. We apply the above-described theoretical model of the FERB to several experimental low-temperature PL and CL spectra of *n*-GaN. A representative HVPE GaN layer, with a thickness of about 25 μm, has been chosen. The GaN layer was unintentionally doped with a typical degenerate interface sublayer with a free-electron concentration $n_{\mathrm{RS}}=2.7\times10^{19}\,\mathrm{cm}^{-3}$ determined by micro-Raman scattering measurements of the film cross section, and a low-doped better-quality part of the layer with carrier concentration less than $10^{17}\,\mathrm{cm}^{-3}$. More experimental details concerning such samples are described elsewhere.[15,16]

To calculate the FERB shape and energy position, in Eqs. (1)–(7) we use the carrier effective-mass values,[18,21] dielectric constant, band gap, and spin-orbit split-off band energy,[21] and the lattice temperature of the experiment as

fixed parameters. Using a standard regression procedure, we vary the free-electron concentration n, electron and hole temperatures, and the ionized impurity concentration N_i. In order to verify the model, we compare the best-fit obtained values of n and N_i with independently measured ones. Since the described procedure is an analytical procedure, it is not necessary to use sample parameters, known or measured independently.

The spatially resolved micro-CL spectrum, taken at $T=7$ K in a highly conducting GaN-sapphire interface region of the cross section of the film, is shown in Fig. 9 (curve *1*, solid line). The experimental spectra were corrected for the CL system response, which is necessary for a spectral band fitting. Curve *2* (dotted line) presents the FERB emission simulated in the nonquasiequilibrium case, and the parabolic approximation as we showed in our earlier work.[16] The best fit to the spectrum has been obtained for the electron concentration $n_{\mathrm{FERB}}=2.5\times10^{19}\,\mathrm{cm}^{-3}$, showing a good agreement with the Raman scattering value even using this simplified model. The calculated FERB emission in the nonparabolic nonquasiequilibrium approximation is shown by curve *3* (dashed line). The best fit of the calculated spectra with the experimental one is obtained for the Fermi energy $E_f=140$ meV and $G=95$ meV and this corresponds to an electron concentration $n_{\mathrm{FERB}}=2.65\times10^{19}\,\mathrm{cm}^{-3}$ according to Figs. 5 and 3, respectively, with a compensation ratio lower than 0.1 and an electron temperature $\Theta=52$ K. The value of the electron concentration, determined by taking into account all corrections in Eqs. (13)–(16), is in a very good agreement with the value ($n_{\mathrm{RS}}=2.7\times10^{19}\,\mathrm{cm}^{-3}$) measured by Raman scattering, indicating the accuracy of the analysis.

We point out that the simulated curves match perfectly the experimental spectra except for the longer-wavelength range at low intensity. Usually in these regions the effect of adjacent emission lines appears. The mismatch is stronger when overlapping takes place, and the latter makes the detailed spectral shape modeling more complicated. The observed discrepancy between theory and experiment in this range of energies may arise from the assumption of equal nonequilibrium electron and hole temperatures Θ. In order to adjust the low-energy slope, we simulate a FERB emission assuming higher lifetime variations for the nonequilibrium holes compared with those of the electrons. This assumption reflects a higher effective hole temperature Θ_h in the Fermi-Dirac function $f_p(E_p)$ in Eq. (1), and it is reasonable bearing in mind that the nonequilibrium holes are spatially localized in the valence-band potential relief and their energy dispersion is stronger. Curve *4* (dashed line) in Fig. 9 presents a spectral shape calculated assuming $\Theta_h=100$ K. The electron temperature is kept the same at $\Theta_e=52$ K. We can see that the low-energy side rises, but is still lower than the experimental one. A better agreement could be obtained if we also take into account the possibility that some of the electrons occupy deeper and thus larger wells in the fluctuations of the band edges. Deeper states in the conduction-band tails could be created also by defect levels, which are specific for the studied samples and thus not reflected by the Eq. (10), where only the Gaussian fluctuations of the shallow impurities are taken into account. Such deeper tail states (see the DOS discussion of Fig. 4) could lead to different recombination kinetics. In general, the latter can not be considered in the framework of the FERB model, because in such a case the electrons should be localized. The contribution of such donor-acceptor-like recombination can be derived by spectral kinetics measurements. Due to the different kinetics of the recombination transitions related to the low-energy part of the spectrum, its intensity can be affected in a different way. Their neglect in the modeling does not decrease the accuracy of the method. Moreover, in some GaN NBE spectra,[25] the emission intensity in the discussed spectral region is much lower. Additionally, the observed discrepancy may also rise due to contributions either from the LO-phonon replica lines or sometimes additional acceptor-bound exciton lines,[32] or from structural defect-related PL emission at $\sim$3.42 eV,[33] which are also neglected in the FERB analysis.

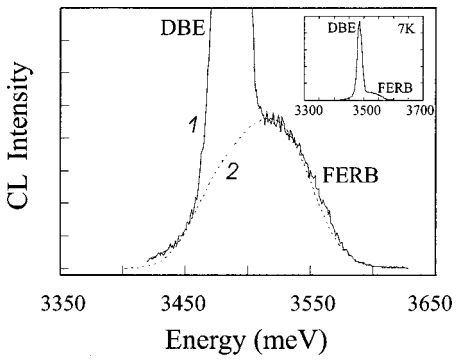

FIG. 10. Low-temperature (7 K) spatially resolved CL spectrum (curve *1*, solid line) taken in a nonuniform area of thick GaN film (Ref. 14). Calculated FERB emission (curve *2*, dotted line) in the nonparabolic approximation for $n=1.95\times10^{19}\,\mathrm{cm}^{-3}$ and $\theta=52$ K. The inset shows the full near-band-edge spectrum.

It is worth noting that the experimental emission spectra (Fig. 9, curve *1*) do not show any peculiarities which could be attributed to a contribution from the light hole recombination. In the corresponding energy range around 3640 meV, the modeled curves are in reasonable agreement with the experimental spectra. A possible explanation of the absence of this influence is based on the larger *e-h* radiative recombination lifetime of light holes, compared to the thermal localizing time of the nonequilibrium heavy holes, as well as on their lower concentration with respect to the heavy-hole concentration. Additionally, the nonequilibrium recombination process can cause a redistribution of light- and heavy-hole concentrations, e.g., nonequilibrium light holes should be able to recombine via the empty acceptorlike valence-band-tail states changing into heavy ones. Such a redistribution is not predicted in the equilibrium and quasiequilibrium approach.

The emission spectra of the unintentionally doped samples sometimes overlap with a strong excitonic peak,[15,16,26,27] and a detailed spectral shape analysis requires a deconvolution procedure. A simpler solution would be similar modeling of the FERB derived from the NBE emission spectra consisting of both the excitonic emission band and underlying broad emission. A similar procedure was

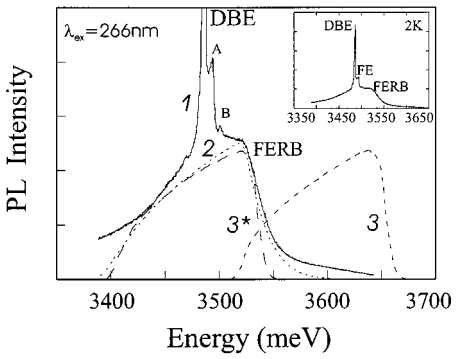

FIG. 11. Low-temperature (2 K) PL spectrum (curve *1*, solid line). Curve *2* (dotted line) is a simulated FERB emission in the nonquasiequilibrium, nonparabolic approximation at $T=2$ K for an electron concentration of $n=2.7\times10^{19}\,\mathrm{cm}^{-3}$. Curve *3* (dashed line) is a calculated FERB emission for the same parameters in quasiequilibrium approximation. Curve *3** presents curve *3* numerically shifted to $-2^{1/2}$ G. The inset shows the full near-band-edge spectrum.

shown in our previous study[16] using the simulated FERB emission in a parabolic approximation. In Fig. 10 we show such experimental CL spectrum (curve *1*, solid line) taken in an intermediate area between the degenerate and good-quality parts of the same layer. The simulated FERB in the nonparabolic approach (curve *2*, dotted line) is also shown in the figure. The best fit value of $E_f=100$ meV and corresponding $G=65$ meV (see Fig. 3) result in a value of free carrier concentration $n_{\mathrm{FERB}}^{\mathrm{non}}=1.95\times10^{19}\,\mathrm{cm}^{-3}$. This result is in a good agreement with the electron concentration value ($n_{\mathrm{RS}}=2.7\times10^{19}\,\mathrm{cm}^{-3}$) determined by Raman scattering although there is a slightly higher mismatch compared to the results shown in Fig. 9 due to the mixed character of the material.

In Fig. 11 we show an experimental PL spectrum of the same GaN film taken at 2 K (curve *1*, solid line) with similar overlapping of excitonic and broad band. The calculated FERB spectrum in the nonparabolic case (curve *2*, dotted line) has been obtained using the following parameters: $E_f=136$ meV, $n_{\mathrm{FERB}}^{\mathrm{non}}=2.7\times10^{19}\,\mathrm{cm}^{-3}$, $G=68$ meV, and $\Theta=13$ K. The latter allows us to achieve the best agreement with the RS data ($n_{\mathrm{RS}}=2.7\times10^{19}\,\mathrm{cm}^{-3}$). The higher carrier temperature used in the simulated spectra is of importance for achieving a good fit to the experimental one, although it has a minor influence on the estimated value of carrier concentration. Based on our results, the fitting procedure for the FERB shape adjustment is sensitive to this parameter in a range of 2–3 K. Moreover, it is a reasonable process in our case, keeping in mind that both equilibrium and nonequilibrium electrons participate in the radiative recombination process. Thus for the total carrier concentration in range of $10^{19}\,\mathrm{cm}^{-3}$, the critical carrier density for internal thermalisation n_c is in the range of $10^{16}\,\mathrm{cm}^{-3}$,[18,31] and the condition for internal thermalisation $n>n_c$ is satisfied.

In addition, in Fig. 11 we also show an emission spectrum simulated in the quasiequilibrium approach (curve *3*) for comparison. The modeling can be performed following Eq. (1) where $p(E_p)$ corresponds to curve *3v* (dashed line) in Fig. 6 (left). The emission band calculated with similar parameters to that used for curve *2* appears at rather higher spectral energies. The spectrum can be shifted to the low-energy side via numerical band-gap renormalization. Although this simple procedure can sometimes be carried out with reasonable accuracy, a discrepancy between the experimental (curve *1*) and calculated (curve 3*) emission shapes can clearly be seen.

V. CONCLUSIONS

We presented a theoretical analysis of the FERB in *n*-GaN, and a comparison with experimental emission spectra. The model assumes free-to-bound transitions between free electrons and holes localized in the maxima close to the valence band created by potential fluctuations. We presented a detailed justification of all elements of our model which includes the effects of band-gap renormalization, band tailing, nonparabolicity, localization, impurity and electron concentration, and temperature.

The model was applied to cathodoluminescence and photoluminescence spectra in GaN. It yielded accurate (to within few percent) values of electron concentration and an estimate of the compensation ratio. The model can be usefully employed for $n>1\times10^{18}\,\mathrm{cm}^{-3}$. The fit of the spectral shape yields *n* and *K*, which can be independently verified from the position of the high-energy edge of the FERB band. The complete method simulation program to calculate the FERB shape and energy position is available free of charge at http://www.phys.uni-sofia.bf/~arnaudov/.

ACKNOWLEDGMENTS

This work was partly supported by the European Community via CLERMONT Project No. HPRN-CT-1999-00132. Dr. P.P. Paskov, A. Isusov, and Dr. L. Vasilev are gratefully acknowledged for fruitful discussions.

[1] B. G. Amaudov, V. A. Vilkotskii, D. S. Domanevskii, S. K. Evtimova, and V. D. Tkachev, Fiz. Tekh. Poluprovodn. **11**, 1799 (1977) [Sov. Phys. Semicond. **11**, 1054 (1977)].

[2] J. De-Sheng, Y. Makita, K. Ploog, and H. J. Queisser, J. Appl. Phys. **53**, 999 (1982).

[3] D. M. Szmyd, P. Porro, A. Mejerfield, and S. Lagomarsino, J. Appl. Phys. **68**, 2367 (1990).

[4] T. Lidekis and G. Treideris, Semicond. Sci. Technol. **4**, 938 (1989).

[5] M. Bugajski and W. Lewandowski, J. Appl. Phys. **57**, 521 (1984).

[6] R. Schwalbe, A. Haufe, V. Gottshaft, and K. Unger, Solid State Commun. **58**, 485 (1986).

[7] N. S. Averkiev, B. N. Kalinin, A. V. Losev, A. A. Rogachev, and A. S. Filipchenko, Phys. Status Solidi A **121**, K129 (1990).

[8] E. Burstein, Phys. Rev. **93**, 632 (1954); T. Moss, Proc. Phys. Soc. London, Sect. B **67**, 755 (1954).
[9] W. van Roosbroeck and W. Shockley, Phys. Rev. **94**, 1558 (1954).
[10] P. van Mieghem, Rev. Mod. Phys. **64**, 755 (1992).
[11] B. I. Shklovskii and A. L. Efros, *Electronic Properties of Doped Semiconductors* (Springer-Verlag, Berlin, 1984), Chap. 11.
[12] E. O. Kane, Phys. Rev. **131**, 79 (1963).
[13] J. I. Pankove, *Optical Processes in Semiconductors* (Prentice-Hall, Inc., Engelwood Cliffs, NJ, 1971), Chap. 6.
[14] E. M. Goldys, T. Paskova, I. G. Ivanov, B. Arnaudov, and B. Monemar, Appl. Phys. Lett. **73**, 3583 (1998).
[15] T. Paskova, E. M. Goldys, R. Yakimova, E. B. Svedberg, A. Henry, and B. Monemar, J. Cryst. Growth **208**, 18 (2000).
[16] B. Arnaudov, T. Paskova, E. M. Goldys, R. Yakimova, S. Evtimova, I. G. Ivanov, A. Henry, and B. Monemar, J. Appl. Phys. **85**, 7888 (1999).
[17] V. L. Bonch-Bruevich, in *Physics of III-V Compounds*, Semiconductors and Semimetals Vol. 1, edited by R. K. Willardson and A. C. Beer (Academic New York, 1966), Chap. 4.
[18] F. Binet and J. V. Duboz, Phys. Rev. B **60**, 4715 (1999).
[19] E. O. Kane, J. Phys. Chem. Solids **1**, 249 (1957).
[20] R. Stepniewski, M. Potemski, A. Wysmolek, K. Pakula, J. M. Baranowski, J. Lusakowski, I. Grzegory, S. Porowski, G. Martinez, and P. Wyder, Phys. Rev. B **60**, 4438 (1999).
[21] O. Madelung, *Semiconductors—Basic Data* (Springer, New York, 1996), p. 86.
[22] K. Seeger, *Semiconductor Physics* (Springer-Verlag, Berlin, 1985).
[23] A. P. Levaniuk and V. V. Osipov, Fiz. Tekh. Poluprevodn. **7**, 1803 (1973) [Sov. Phys. Semicond. **7**, 1058 (1973)].
[24] B. Arnaudov and A. Isusov, in *Proceedings IC on Optical Characterization of Semiconductors, Satellite Conference of the 20th International Conference on the Physics of Semiconductors, Sofia, Bulgaria, August 2–4, 1990*, edited by B. B. Kushev (Trans Tech Zurich), p. 151.
[25] F. Bertram, T. Riemann, J. Christen, A. Kaschner, A. Hoffmann, C. Thomsen, K. Hiramatcu, T. Shibata, and N. Sawaki, Appl. Phys. Lett. **74**, 359 (1999).
[26] F. Bertram, T. Riemann, J. Christen, A. Kaschner, A. Hoffmann, K. Hiramatcu, T. Shibata, and N. Sawaki, Mater. Sci. Eng., B **59**, 117 (1999).
[27] M. Leroux, B. Beaumont, N. Grandjean, P. Lorenzini, S. Haffouz, P. Vennegues, J. Massies, and P. Gibart, Mater. Sci. Eng., B **50**, 97 (1997).
[28] I.-H. Lee, J. J. Lee, P. Kung, F. J. Sanches, and M. Razegi, Appl. Phys. Lett. **74**, 102 (1999).
[29] B. Monemar, in *Gallium Nitride (GaN) I*, Semiconductors and Semimetals Vol. **50**, edited by J. I. Pankove and T. D. Moustakas (Academic, New York, 1988), Chap. 11.
[30] E. Liopoulos, D. Doppalapudi, H. M. Ng, and T. D. Moustakas, Appl. Phys. Lett. **73**, 375 (1998).
[31] J. Shah, Solid-State Electron. **21**, 43 (1978).
[32] G. Pozina, J. P. Bergman, T. Paskova, and B. Monemar, Appl. Phys. Lett. **75**, 4124 (1999).
[33] G. Salviati, M. Albrecht, C. Zanotti-Freganara, N. Armani, M. Mayer, Y. Schreter, M. Guzzi, Yu. V. Melnik, K. Vassilevski, V. A. Dmitriev, and H. P. Strunk, Phys. Status Solidi A **171**, 325 (1999).